

Article

Antibacterial and Photocatalytic Dye Degradation Activities of Green Synthesized NiSe Nanoparticles from *Hibiscus rosa-sinensis* Leaf Extract

Lakshmi Velayutham ¹, C. Parvathiraja ², Dhivya Christo Anitha ¹, K. Mahalakshmi ¹, Mary Jenila ^{1,*}, Jeetendra Kumar Gupta ³, Saikh Mohammad Wabaidur ⁴, Masoom Raza Siddiqui ⁴, Sikandar Aftab ⁵ and Wen-Cheng Lai ^{6,7,*}

¹ Department of Physics, St. Xavier's College (Autonomous), Palayamkottai, Manonmaniam Sundaranar University, Tirunelveli 627012, Tamilnadu, India

² Department of Physics, Manonmaniam Sundaranar University, Tirunelveli 627012, Tamilnadu, India

³ Institute of Pharmaceutical Research, GLA University Mathura, Mathura 281406, Uttar Pradesh, India

⁴ Chemistry Department, College of Science, King Saud University, Riyadh 11451, Saudi Arabia

⁵ Department of Intelligent Mechatronics Engineering, Sejong University, 209 Neungdong-ro, Gwangjin-gu, Seoul 05006, Republic of Korea

⁶ Bachelor Program in Industrial Projects, National Yunlin University of Science and Technology, Douliu 640301, Taiwan

⁷ Department of Electronic Engineering, National Yunlin University of Science and Technology, Douliu 640301, Taiwan

* Correspondence: jenilason@gmail.com (M.J.); wenlai@yuntech.edu.tw or wenlai@mail.ntust.edu.tw (W.-C.L.)

Abstract: Ecosystems worldwide face a serious and life-threatening water crisis due to water contamination. Nanotechnology offers a promising solution to this issue by providing methods for removing pollutants from aquatic sources. In this study, we utilized a green and simple approach to biosynthesize NiSe NPs using *Hibiscus rosa-sinensis* extract as the bio-source. The plant extract acts as a reducing, stabilizing, and capping agent in the synthesis process. A simple hydrothermal method was employed to blend the NiSe NPs photocatalysts. UV-Visible DRS spectroscopy was utilized to confirm the reduction in and stabilization of Ni²⁺ and Se²⁻ ions. The resulting NiSe NPs have a bandgap of 1.74 eV, which facilitates electron and hole production on their surfaces. To characterize the functional groups on the NiSe NPs and their surface interactions with bio-compounds, FTIR spectroscopy was utilized. XRD analysis revealed the crystallite size of the NiSe NPs to be 24 nm, while FE-SEM and TEM imaging showed their spherical shape and material distribution. EDX spectroscopy confirmed the integrity of the NiSe NPs' material. XPS analysis provided information on the chemical composition, nickel and selenium valency, and their interface. The efficacy of the NiSe NPs as a blended photocatalyst in photodegrading Methylene Blue (MB) dye was tested under visible light, resulting in 92% degradation. Furthermore, the NiSe NPs exhibited bactericidal activity against *Escherichia coli* and *Staphylococcus aureus* bacteria due to their advanced oxidation and reduction in charge particles, which increased the degradation efficiency and suppressed cell proliferation. Based on the obtained findings, the NiSe NPs show promise as a powerful agent for water remediation and microbial resistance.

Keywords: green synthesis; NiSe; nanoparticles; photocatalysis; degradation and antibacterial resistance



Citation: Velayutham, L.; Parvathiraja, C.; Anitha, D.C.; Mahalakshmi, K.; Jenila, M.; Gupta, J.K.; Wabaidur, S.M.; Siddiqui, M.R.; Aftab, S.; Lai, W.-C. Antibacterial and Photocatalytic Dye Degradation Activities of Green Synthesized NiSe Nanoparticles from *Hibiscus rosa-sinensis* Leaf Extract. *Water* **2023**, *15*, 1380. <https://doi.org/10.3390/w15071380>

Academic Editor: Andreas Angelakis

Received: 12 March 2023

Revised: 27 March 2023

Accepted: 1 April 2023

Published: 3 April 2023



Copyright: © 2023 by the authors. Licensee MDPI, Basel, Switzerland. This article is an open access article distributed under the terms and conditions of the Creative Commons Attribution (CC BY) license (<https://creativecommons.org/licenses/by/4.0/>).

1. Introduction

As the world's population grows, so does the demand for consumer products. Additionally, the production of colored products increases day by day, resulting in severe atmospheric pollution. The issue of water pollution is one of the most serious environmental issues of the present and the future. Most water contamination is caused by organic

contaminants, dyes, and heavy metals. Among the main sources of these contaminants in water are the pharmaceutical, textile, dyeing, and metallurgical industries. Textile, leather, pharmaceuticals, and paper mill waste are among the leading polluters of water, posing severe hazards to human and environmental health. The three main types of dyes are acid dyes, basic dyes, and vat dyes [1]. The most harmful dyes are cationic dyes, which are tough on receiving water's ecology [2]. The cationic dye methylene blue (MB) is often called methylthioninium chloride and belongs to the thiazine family. It has adverse consequences for both the environment and humans [3]. Moreover, due to their complex aromatic structure, these dyes are difficult to degrade in the atmosphere, resulting in serious water contamination and civic health problems such as allergic dermatitis, skin irritation, cancer, mutation, and genetic effects on marine life and humans [4,5].

In the treatment of wastewater, various chemical, physical, and biological methods have been utilized, including filtration, advanced oxidation, flocculation, chemical precipitation, solvent extraction, nanofiltration, ion exchange, ozonation, electrochemical techniques, coagulation, catalysis, photodegradation, chemical degradation, and adsorption [6–11].

Additionally, several of these systems have disadvantages such as high operational costs, secondary sludge generation, and a greater use of electricity and chemicals [12]. Photocatalytic dye degradation generates no sludge, reduces undesirable odors, and may produce byproducts [13]. The photocatalytic treatment is one of the most studied dye removal techniques due to its great effectiveness, nontoxicity, low cost, and ease of removal [14]. There are many materials that are commonly used as photocatalysts, including biosorbents, zeolites, multiwalled carbon nanotubes, cellulose-based activated carbon, ZnS, CdTe, TiO₂, ZnO, CdS, SnO₂, HgS, and selenide [15–21]. The higher band gap of semiconductors (3 eV) and lower catalytic harvesting efficiency make them less efficient at utilizing solar light or separating charges. The fascinating physical and chemical characteristics of selenium (Se)-based materials have drawn considerable attention in the past few years, as they have a low bandgap, and are regarded as a key family of semiconducting chalcogenides [22].

A number of metal selenides are commonly used as photocatalysts, including CdSe, ZnSe, PbSe, CuSe, HgSe, and NiSe₃ [23–27]. The unique characteristics of nickel selenide have attracted tremendous interest around the world. Several applications can be made with nickel selenide due to its attractive magnetic and electrical properties, including solar cells, conductivity, and sensors [28,29]. Nickel selenide (NiSe) is the most widely applied class of materials with applications in electrocatalysts [30], supercapacitors [31], sensors [32], electrolysis [33], optical applications [34], photocatalysts [27], and Dye-Sensitized Solar Cells (DSSCs) [35]. *Hibiscus rosa-sinensis* is a species of Malvaceae found in abundance in the Western Ghats of India, especially in Tamilnadu. *Hibiscus rosa-sinensis* is traditionally known as shoeblack pant in Tamil. Due to its good medicinal value, its leaves are used to treat gastrointestinal disorders such as gastric ulcers and stomach pain [36–39]. Among the active chemicals found in *Hibiscus rosa-sinensis* leaf extracts are alkaloids, tannins, flavonoids, and phenols [40]. We present herein a green method to synthesize nickel selenide NPs using *Hibiscus rosa-sinensis* as the source of metals and metal oxides such as Fe₂O₃, Ag, CuI, and Ag/ZnO [41–45]. Green synthesis of NPs refers to a novel approach of producing NPs using plant extracts or other natural sources, such as fungi and bacteria, rather than conventional chemical methods. The process has several advantages, such as being eco-friendly, cost-effective, and sustainable. However, there are also some limitations to this method that need to be considered. One major limitation is the lack of control over the size and shape of the NPs. The composition and concentration of the plant extracts or other natural sources used can vary, resulting in a wide range of sizes and shapes of NPs, which can affect their properties and applications. Another limitation is the reproducibility and scalability of the process. The composition of the plant extracts or other natural sources used can vary between batches, resulting in inconsistencies in the size, shape, and quality of the NPs [46]. Additionally, the process may not be scalable to large-scale production, which can limit its potential applications. Another limitation is the potential toxicity

and stability issues associated with the NPs produced. Plant extracts and other natural sources may contain impurities or compounds that can affect the properties and stability of the NPs. The potential toxicity of these NPs to human health and the environment is not yet fully understood. Finally, the scope of applications of green synthesis NPs may be limited compared to those produced by conventional chemical methods due to their different properties and functionality. Despite these limitations, green synthesis of NPs is a promising approach for the development of eco-friendly and sustainable nanomaterials. Further research is needed to overcome these limitations and improve the reproducibility, scalability, and safety of the process.

NiSe NPs have several identification gaps that require further research. Firstly, the crystal structure of the NiSe NPs is not yet fully understood, and more studies are needed to determine the exact crystal structure and its correlation with the properties of the NPs. Additionally, synthesizing the NiSe NPs with well-controlled size and shape is still a challenge, and further research is necessary to develop effective synthesis methods that can produce NPs with specific size and shape. Furthermore, the surface chemistry of NiSe NPs, which includes surface energy, surface charge, and surface functionalization, can have a significant impact on their properties and applications, and more research is needed to understand the surface chemistry of the NiSe NPs and develop methods for controlling their surface properties. The stability and reactivity of the NiSe NPs under different environmental conditions are not well understood, and more studies are necessary to investigate their stability and reactivity and potential applications in various fields. Lastly, the toxicity and biocompatibility of the NiSe NPs are important factors to consider for their potential use in biomedical applications, and more research is needed to understand their toxicity and biocompatibility and develop methods for minimizing any potential adverse effects. A wide range of characterization techniques were employed to analyze the synthesized nickel selenide NPs, including XRD, FTIR, UV-DRS, FE-SEM, TEM, EDX and XPS. This study examined the degradation of MB dye and resistance to noxious bacteria by nickel selenide.

2. Materials and Methods

2.1. Synthesized Materials

In this experiment, nickel chloride ($\text{NiCl}_2 \cdot 6\text{H}_2\text{O}$) and selenium powder (90% Sigma-Aldrich) were purchased from Sigma-Aldrich and used without supplemental distillation. Leaves of *Hibiscus rosa-sinensis* were collected from Tirunelveli in fresh and healthy condition.

2.2. Preparation of *Hibiscus rosa-sinensis* Leaf Extract

In order to remove any foreign contaminants, the leaves collected from *Hibiscus rosa-sinensis* were washed several times with distilled water before being used. The cleaned leaves were dried in air for ambient temperature for 24 h. The leaves were chopped into fine powder using an oxidized knife. A mixture of 100 mL of double-distilled water and 100 mg of these chopped *Hibiscus rosa-sinensis* leaves was then heated at 120 °C for two hours. As soon as the final solution was collected, it was filtered and saved for further preparation of the NPs.

2.3. Synthesis of NiSe NPs

A stoichiometric molar ratio of nickel chloride (0.5 g) and Selenium powder (0.5 g) was mixed with 10 mL plant extract in a 250 mL beaker and stirred for an hour. The color of the mixture changed when it delivered the initiation of reaction. The solution was powdered and put into a thermal reactor for 24 h at 120 °C. After centrifuging the solution, it was calcined for two hours at 500 °C. After washing and drying the precipitate, it was kept for further analysis [47].

2.4. Characterization of NiSe NPs

Optical efficiency of the NiSe NPs was capitalized from UV-Visible DRS spectroscopy (Shimadzu-2600, Kyoto, Japan). Fourier transform infrared (FTIR)-spectra were obtained in the range from 4000 to 400 cm^{-1} using a (PerkinElmer, Waltham, MA, USA) spectrophotometer. Powder XRD analysis was conducted using an X-ray diffractometer (X-Pert Pro, Overijssel, The Netherlands) (2θ range 20–80°), 40 kV, 30 mA Cu K alpha radiations with the wavelength of 1.540 Å. Field Emission Scanning electron microscopy (FE-SEM) coupled with energy dispersive X-ray (EDX) analysis of the NiSe NPs was carried out using a Carl Zeiss Field Emission Scanning Electron Microscopy (FE-SEM) coupled with EDAX with an accelerating voltage of 25 kV. Transmission electron microscopy (TEM) was carried out using Titan (Julich, Germany). Binding energy of the NiSe NPs was examined from X-ray photoelectron spectroscopy (XPS, PHI 5000 Versa Probe III, Physical Electronics, Chanhassen, MN, USA).

2.5. Bacterial Suspension

In an antibacterial test, *Escherichia coli* 745 and *Staphylococcus aureus* 9779 were utilized as sources of microorganisms. *E. coli* is a gram-negative bacterium, whereas *S. aureus* is a gram-positive bacterium. Both of them were grown in the LB medium for 48 h at 36 °C. The well diffusion method was utilized to test the prepared composite and standard sample. A cork-borer with a diameter of 0.85 cm was used to create a well in the LB medium. Approximately 5 mL of the test sample was then injected into the well and incubated at 36 °C for 24 h. The diameter of the zone of inhibition was used to assess microbial growth. The experiment was repeated five times to determine the mean value. The results were then compared to a standard antimicrobial, streptomycin (20 mm) disc.

2.6. Photocatalytic Degradation Experiment

Using visible light radiation, the NiSe NPs degrade the MB dye. To begin the reaction, 50 mL of MB (1×10^{-5} M) was placed in a 250 mL beaker. To determine the adsorption and desorption kinetics, 0.05 (g) of photocatalyst was added to the solution and left in the dark for 2 h. After 2 h, the solution was exposed to visible light irradiation while being continuously stirred at 550 rpm. The simulate light is almost 10 cm away from the beaker. The aliquot solution was then withdrawn every 10 min, centrifuged, and the rate of dye degradation was measured using an MB spectrophotometer at 654 nm.

The removal percentages % of the dye were determined using the following formula:

$$\text{Percentage (\% of dye removal)} = \frac{C_{\text{MBi}} - C_{\text{MBT}}}{C_{\text{MBi}}} \times 100$$

C_{MBi} —Initial dye concentration of MB dye solution

C_{MBT} —Light-irradiated dye concentration with different time intervals [48,49].

3. Results and Discussion

3.1. UV-Visible DRS Analysis

UV-DRS spectroscopy was used to characterize optical absorption and defects as shown in Figure 1a,b. The optical absorption edge spectra of the green synthesized NiSe NPs are located at 570 nm and describe electron excitation of Ni to the Se element [50]. The NiSe transitions were observed in the visible region and electron excitations were confirmed. In the visible region, electron excitation has a great potential for light harvesting and can effectively infect organic dye bonds [51]. In order to calculate the bandgap, the defect of the NiSe NPs was used. From the Tauc plot in Figure 1b, we can see that the plot is linear and indicates a direct transition. In the NiSe NPs, the bandgap was determined to be 1.74 eV, which is consistent with the previous literature [52,53]. The green synthesized NiSe NPs have a narrow bandgap, which enable control of the release of ions to the target, and increased surface areas, which determine the antibacterial and degradation properties against the toxic elements.

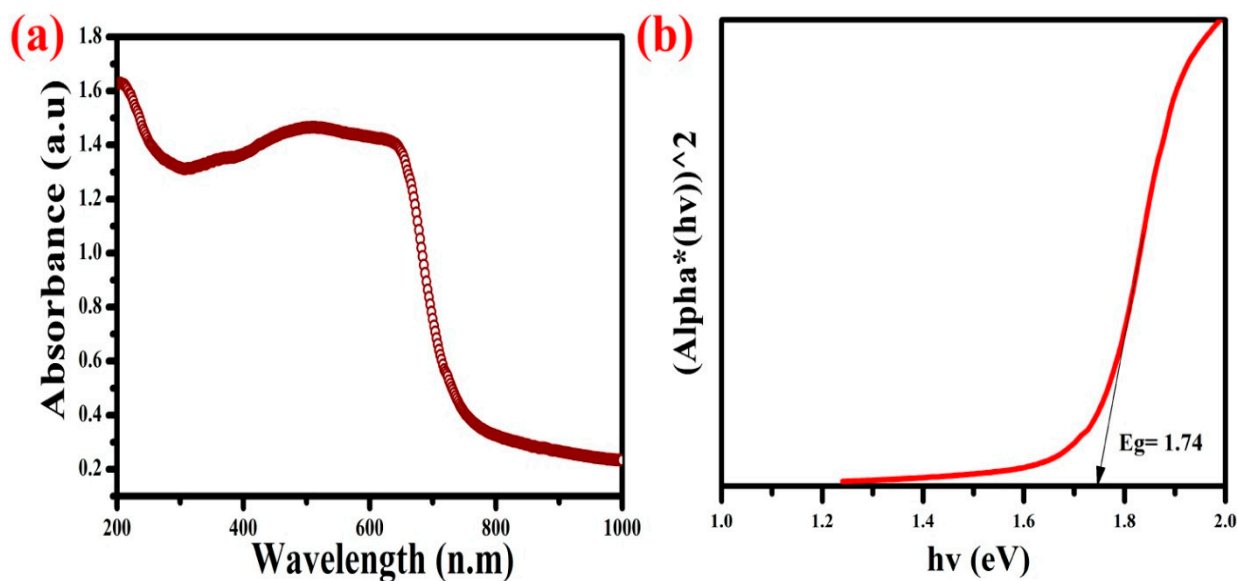


Figure 1. UV-DRS optical absorbance (a) and bandgap (b) spectra of green synthesized NiSe NPs.

3.2. XRD Analysis

Figure 2 represents the X-ray diffraction pattern of green synthesized NiSe NPs. The observed peaks at 2θ values are 32.5° , 44.3° , 50.4° , 59.2° , 61.7° and 69.6° , which corresponds to the (101), (102), (110), (103), (201), and (202) planes, respectively. Diffractive patterns of the green synthesized NiSe NPs are in good agreement with the standard JCPDS card (75-0610) hexagonal crystalline structure of NiSe, and these formations are a result of the interaction between the Ni and Se atoms [54–56]. The phenolic bio-compounds were responsible for the growth of the particles and the construction of their interfaces. Particle formation and nucleation evolution were determined by the lattice parameters, such as strain, size, density, and surface area. Using Scherer's equation, an average particle size of 24 nm was determined. The NiSe NPs synthesized with the smallest crystallite size produced the largest surface area and enhanced lattice strain. As a result of the narrow crystallite size, the electron mitigation toward the conduction band is enhanced and promotes the active sites in degradation.

3.3. FTIR Analysis

Figure 3 shows the FTIR spectroscopy of the green synthesized NiSe NPs. Ni reduction and Se stabilizations were attained from the *Hibiscus rosa-sinensis* plant extracts. The NiSe NPs have a large and intense band at 3558 cm^{-1} . This band is associated with the vibrational modes of the -OH groups bonded to the peripheral hydrogen and atoms of the NiSe NPs structural moieties [57]. The weaker band at 1665 cm^{-1} is associated with the C-H bending vibrations, which come from the amide and amine compounds of plant bio-molecules [58]. The band appearing in the range from 850 to 500 cm^{-1} indicate the occurrences of the NiSe bonds in the NiSe NPs [59]. The composition can affect the broad and asymmetric band centered at 600 and 500 cm^{-1} , which is attributed to the vibrational mode of Se-Metal stretching [60–62]. The Ni and Se stretching bonds are derived from the phase purity of the metal compounds, and their edge was attained by plant bio-nutrients. The bio-nutrients can produce the pure metal selenide compounds with low agglomeration.

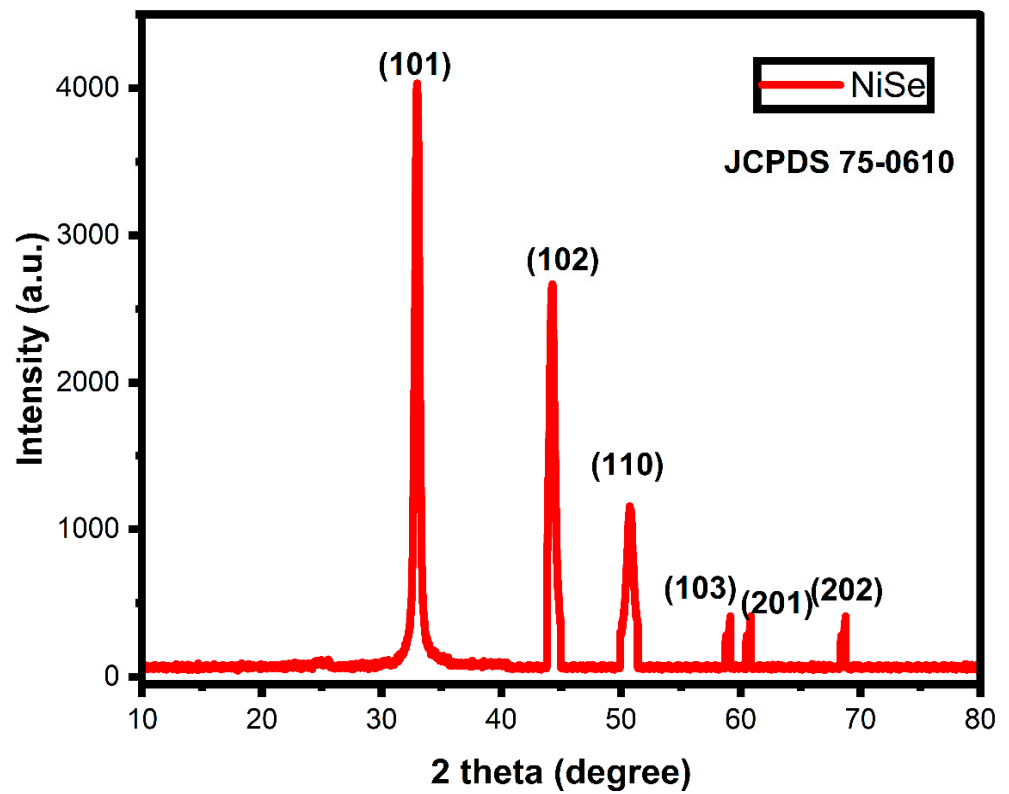


Figure 2. XRD pattern of green synthesized NiSe NPs.

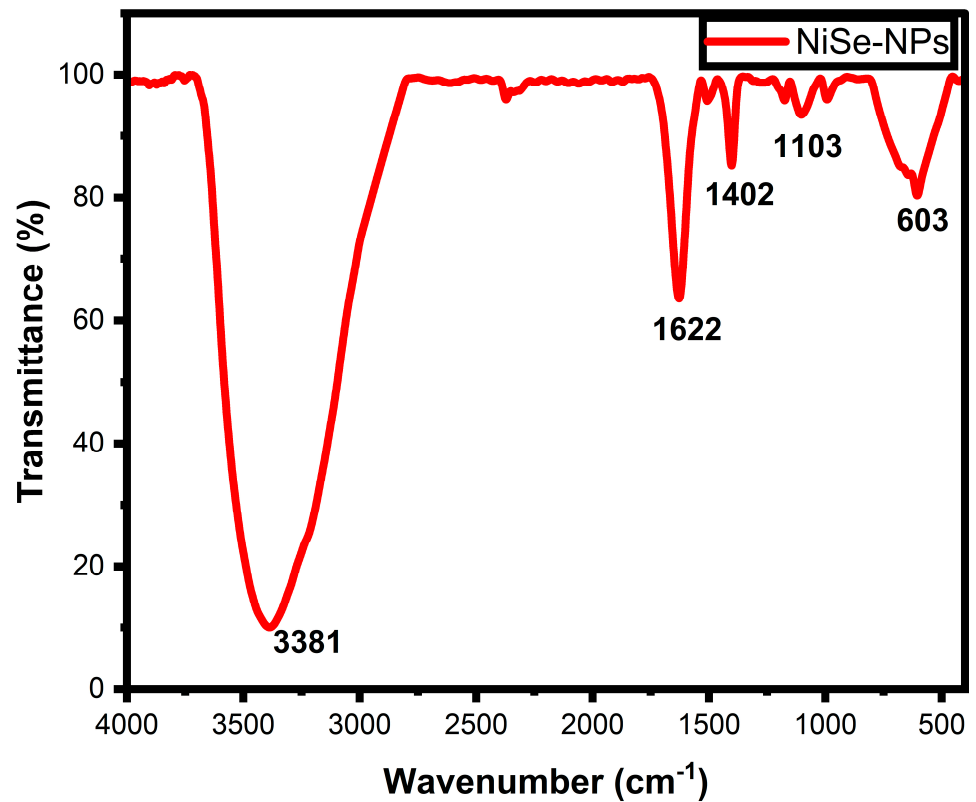


Figure 3. FTIR spectra of green synthesized NiSe NPs.

3.4. FE-SEM with EDX Analysis

The morphological and elemental compositions of the green synthesized NiSe NPs were investigated by field emission-scanning electron microscopy (FE-SEM). Figure 4a,b illustrate the FE-SEM images at the different magnifications. The average diameter of these microspheres is 26 nm, and their spherical particles are not distributed uniformly. The green synthesized NiSe NPs have large aggregated and irregular sphere particles on their surface. The larger surface area and numerous active sites of the aggregated NiSe NPs are responsible for their increased photocatalytic activity [63,64]. The EDAX technique is one of the most commonly used techniques for elemental analysis on the NiSe NPs. EDAX analysis (Figure 4c,d) was performed over the surface of the NiSe NPs for analyze purity, and the non-stoichiometric percentage of Se and Ni implies the accurate crystal arrangement. Finally, the EDAX analysis revealed that only Ni and Se were present in the synthesized materials.

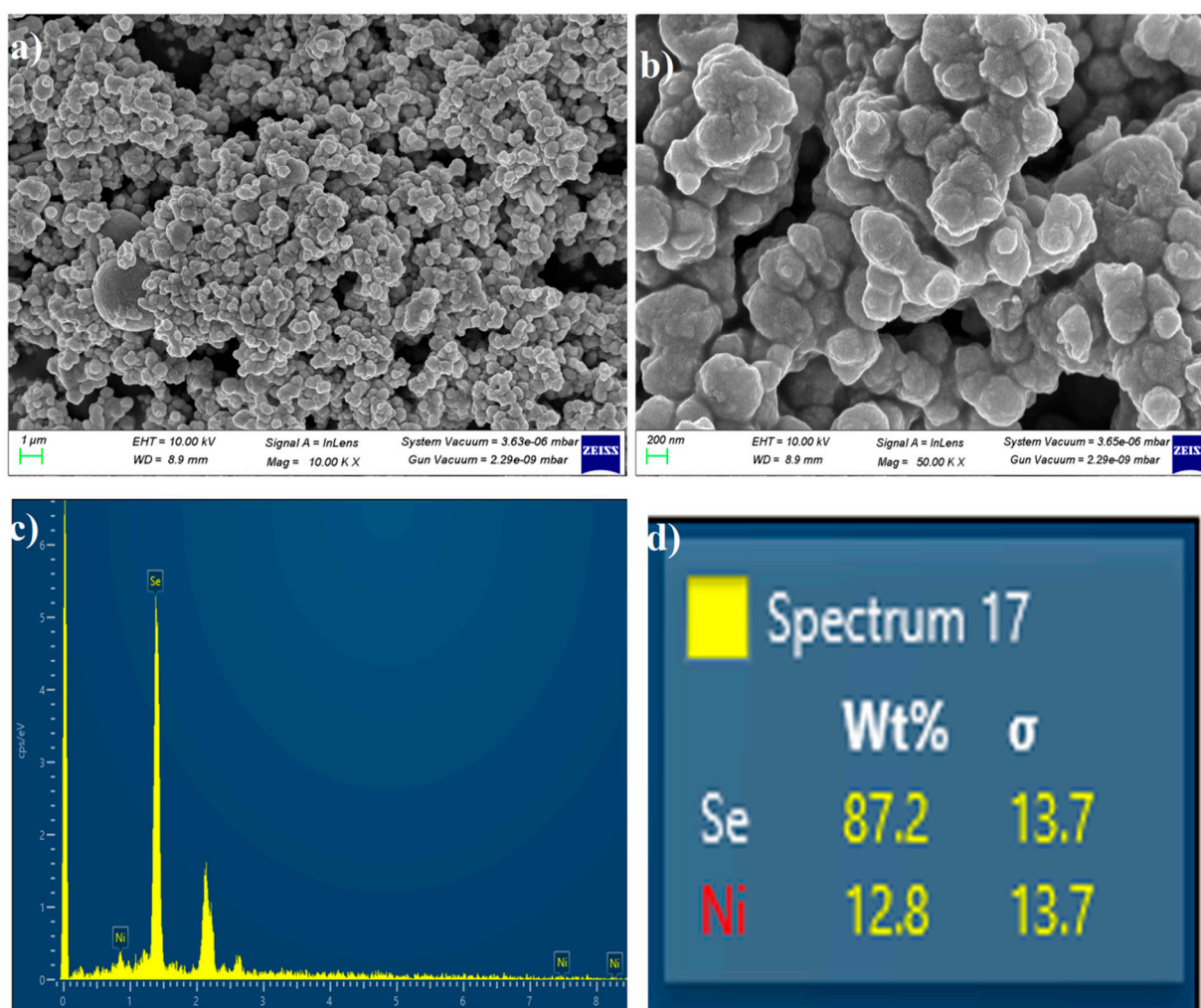


Figure 4. (a,b) SEM and (c,d) EDAX analysis of green synthesized NiSe NPs.

3.5. TEM Analysis

The green synthesized NiSe NPs' surface area, particles size, shape and texture were identified from the TEM analysis and their two different magnified images are shown in Figure 5a,b. The green synthesized NiSe NPs express the spherical shape and oval-like shape particles in the TEM images. The spherical shape particles majorly occupy the surface compared to the oval-like structure. The spherical shapes have reduced the edges and form an oval-like structure. The particles distribution of the NiSe NPs is even with an average size around 24 nm, which well match the crystallite size and their oval-like structure. The

results infer the electron migrations and large surface area of the materials [65,66]. The NiSe NPs of spherical shape re-ensured the narrow bandgap and smallest crystallite size of the green synthesized NiSe NPs.

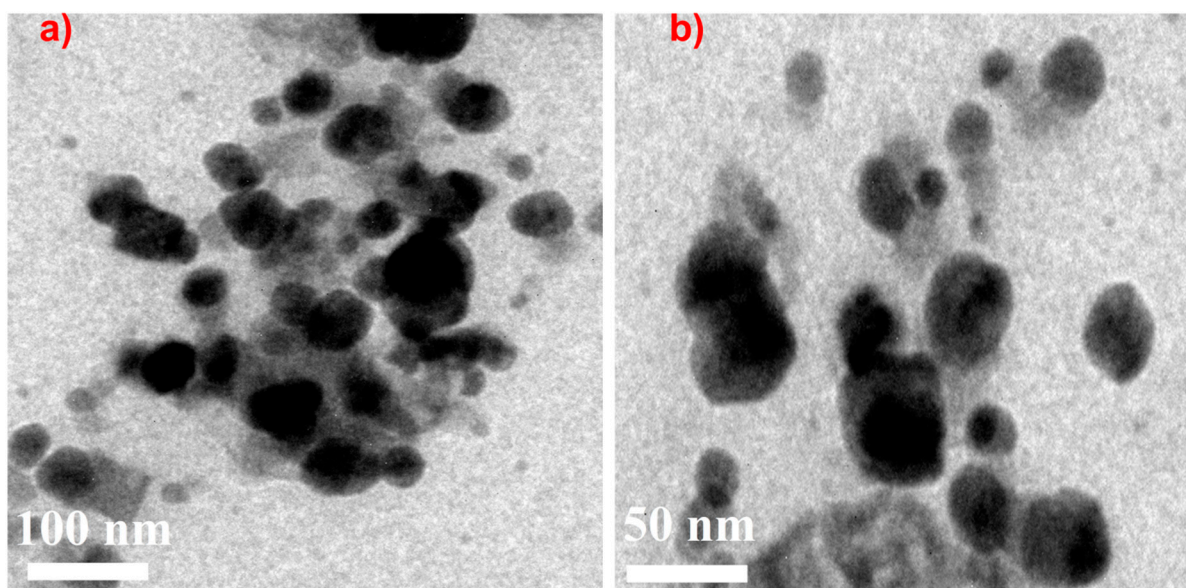


Figure 5. (a,b) TEM images of green synthesized NiSe NPs.

3.6. XPS Analysis

Based on the XPS analysis, the chemical composition and surface cationic electronic state were characterized. The XPS spectrum of the NiSe NPs displays the survey, nickel, selenide, and carbon spectrum in Figure 6a–d. According to the survey spectrum, pure NiSe NPs are present on the catalyst surfaces, showing the presence of nickel and selenide. In the case of the pure nickel elements, the binding energies of 857 eV, 862 eV, 871 eV, and 880 eV correspond to Ni^{3+} [67–69]. Given the Ni existence and its stability with selenide materials, Ni^{2+} is stronger than Ni^{3+} . The Ni^{2+} valency of the nickel elements associated with the Ni-2p state and their splitting energy is Ni-2p_{1/2} and Ni-2p_{3/2}. The binding energies of 54.2 eV (Se-3d_{5/2}) and 55.6 eV (Se-3d_{3/2}) [70–72] were consistent with the NiSe and Se-Se bonds on the NPs. The Se-3d state of the selenium elements indicates that selenium interacts with the cationic metal, and their interface is exposed by the NiSe bonds. Plant bio-fuels formed the interface between the metal and selenide compounds, as shown by the carbon peaks at 285 eV (Figure 6d) [73,74]. The phase pure Ni-2p and Se-3d and their reactions were well matched with the EDX, XRD, and FTIR characterizations.

3.7. Photocatalytic Activity

The photocatalytic activity of the NiSe NPs against the cationic MB dye is shown in Figure 7a–c. The absorbance spectrum at 664 nm (Figure 7a) decreases due to the exposure of light, which clearly indicates the degradation of dye molecule by the generation of the reactive intermediates. The dye photodecomposition involves two phenomenon such as (i) the adsorption and (ii) the photolysis of heterogeneous structure. The photocatalytic dye degradation mechanism of the NiSe NPs involves a process known as photodegradation, which occurs when the catalyst absorbs light and generates electron-hole pairs. These pairs are then utilized in the degradation of organic pollutants. One possible mechanism for this process involves several steps. First, when exposed to light, the NiSe NPs absorb photons and generate electron-hole pairs. These pairs are separated due to the different energy levels of the NiSe NPs, which create a charge imbalance on the surface of the catalyst. Next, the electrons on the surface of the catalyst react with oxygen in the environment to produce superoxide radicals. These radicals react with water molecules to produce

hydroxyl radicals, which are strong oxidizing agents capable of breaking down organic pollutants. The hydroxyl radicals then attack the dye molecules, breaking down their chemical bonds and reducing them into smaller, less harmful molecules such as carbon dioxide and water. Finally, the resulting by-products are either released into the environment or further degraded by other chemical reactions [75–80]. It is important to note that this mechanism is a simplified explanation of the photocatalytic dye degradation process, and that the actual reaction mechanism may involve more complex intermediate steps.

Furthermore, MB might be devoured by these radicals, which have a strong oxidation capacity and can destroy the organic dye matrix into CO₂, oxygen, peroxide, and other fragmental byproducts. Figure 7c shows that after 120 min, the NiSe NPs exhibit 92% degradation of MB. Based on its reduced band gap, high light harvesting efficiency, and restricted electron-hole recombination rate, the NiSe photocatalyst shows superior catalytic activity [81]. The degradation rate of the NiSe NPs follows the pseudo-first-order kinetics and the value is 0.01886 min⁻¹, Figure 7d. The mechanism of the photocatalytic dye degradation is illustrated in Figure 8. In comparison with metal selenide and its associated compounds (Table 1) [82–92], the green synthesized NiSe NPs demonstrated equal degradation performance.

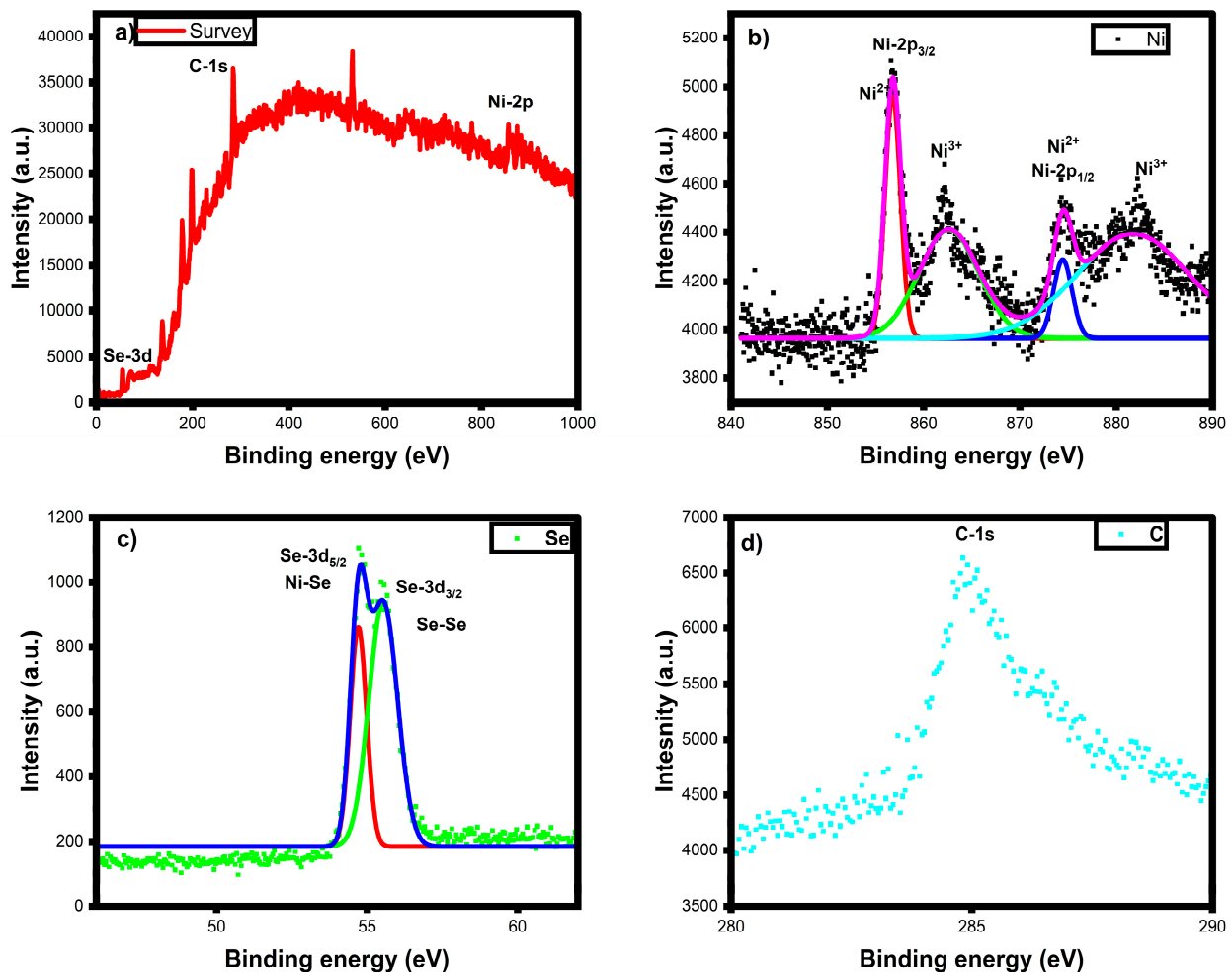


Figure 6. XPS survey (a), Ni-2p (b), Se-3d (c), C-1s (d) spectra of green synthesized NiSe NPs.

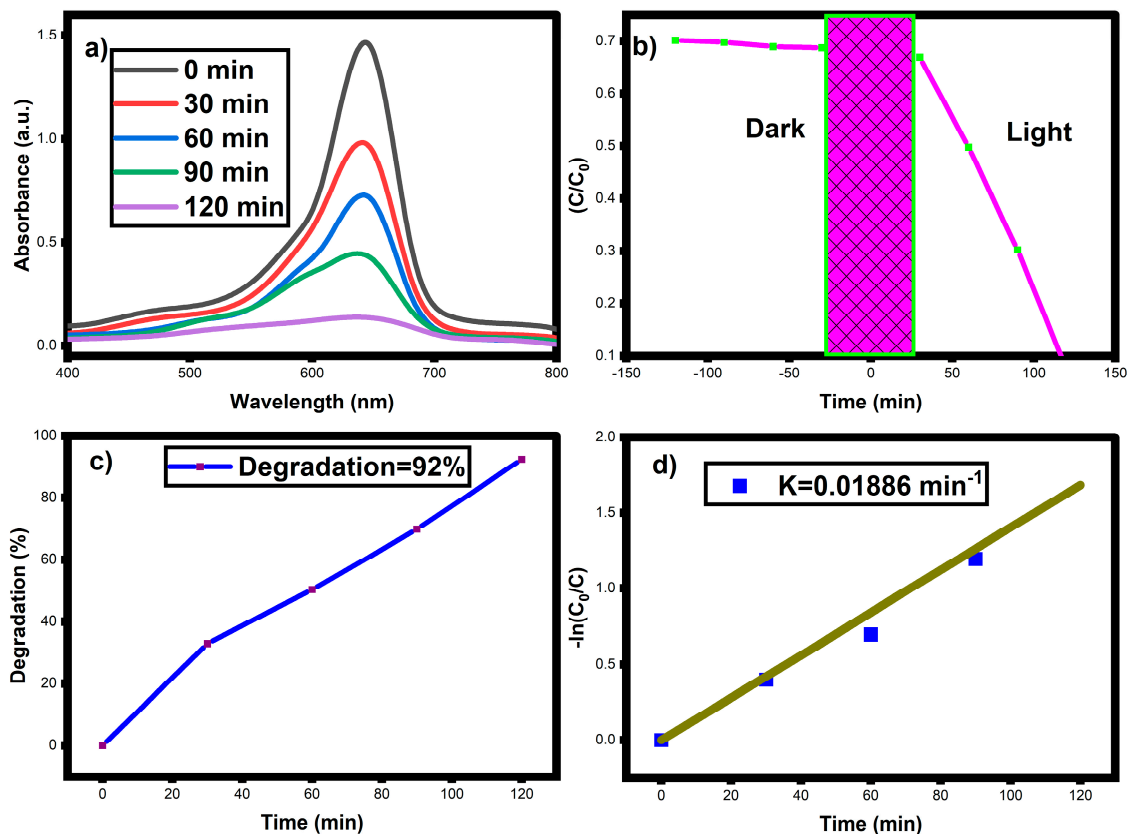


Figure 7. (a) MB dye degradation spectra, (b) Plots of dark and light condition (C/C_0), (c) Degradation efficiency (%) spectra and (d) Plots of $\ln(C_0/C)$ versus reaction time over MB dye molecules using green synthesized NiSe NPs.

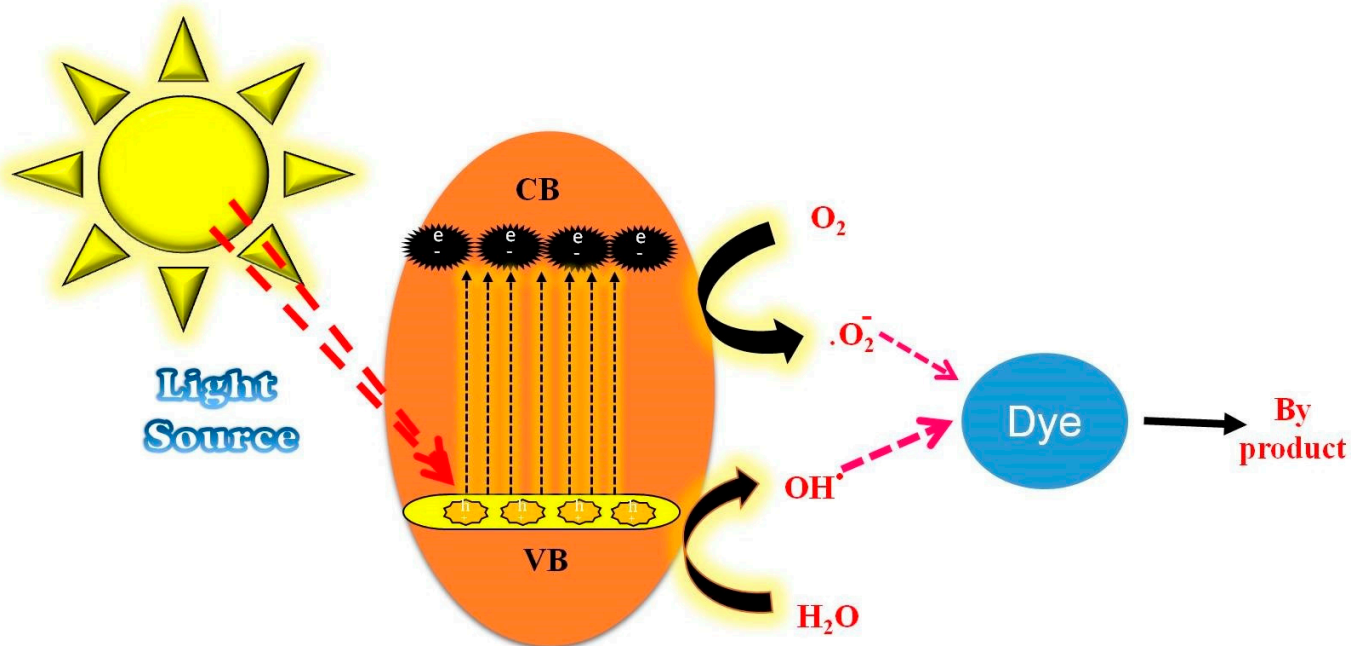


Figure 8. Mechanism of photocatalytic dye degradation of NiSe NPs.

Table 1. Photocatalytic dye degradation comparison table of various Metal-Se-NPs.

Si. No	Material	Dye	Dye Volume	Catalyst Load	Light Source	Efficiency	Ref
1.	PbSe NPs	Rh-B	50 mL	50 mg	50 W- halogen light	82%/30 min	[82]
2.	CuSe 2-x	MB	50 mL	0.1 g	Sunlight	93.4%	[83]
3.	PtSe ₂ /graphene	MB	80 mL	10 mg	Visible light source	95%/180 min	[84]
4.	ZnSe	MO	100 mL	10 mg	XENON LAMP	80%/120 min	[85]
5.	BiSe-CM	CV	20 mL	0.2 g	Natural Sunlight	98%/150 min	[86]
6.	CoSe	Rh-B	50 mL	50 µg/mL	UV light	98%/120 min	[87]
7.	Ag-CdSe/GO@CA	Mg	30 mL	120 mg	300 W mercury lamp light s	97%/25 min	[88]
8.	SnSe	MB	100 mL	0.10 g	Sunlight	98.4%/60 min	[89]
9.	CuSe/MoSe ₂	MB	100 mL	20 mg	250 W high-pressure mercury lamp	95%/120 min	[90]
10.	CdSe-rGO	MB	80 mL	30 mg	8 W-Hg lamps	70%/210 min	[91]
11.	PtSe ₂ -graphene/TiO ₂	Rh-B	80 mL	10 mg	UV light	70%/180 min	[92]
12.	NiSe	MB	50 mL	50 mg	Visible light	92%/120 min	Present work

3.8. Antimicrobial Activity

The antimicrobial activities of the NiSe NPs were investigated against Gram +Ve, *S. aureus* and Gram -Ve, *E. coli* bacteria (Figure 9). The bacteria of *E. coli* 10 mm and *S. aureus* 15 mm exhibit the antimicrobial activity with the standard drug gentamycin when measured against the zone of inhibition (18 mm). *E. coli*, or *Escherichia coli*, is a type of bacteria that is commonly found in the intestines of humans and animals. Most strains of *E. coli* are harmless and even beneficial, aiding in digestion and the production of certain vitamins. However, there are some strains of *E. coli* that can produce toxins that cause foodborne illness. *S. aureus*, or *Staphylococcus aureus*, is a type of bacteria that is commonly found on the skin and in the nose of healthy individuals. While it is generally harmless, certain strains of *S. aureus* can produce toxins that cause food poisoning [93–95]. One such toxin is enterotoxin, which can cause symptoms such as nausea, vomiting, and diarrhea. In severe cases, it can lead to dehydration and require hospitalization. It is important to note that proper food handling and hygiene can help prevent the spread of both *E. coli* and *S. aureus* infections. The antibacterial mechanism of the NiSe NPs is not yet fully understood, but several studies have proposed some possible mechanisms. One such mechanism is the generation of reactive oxygen species (ROS) such as superoxide anion radicals, hydroxyl radicals, and singlet oxygen by the NiSe NPs, which can damage bacterial cell membranes and disrupt intracellular metabolism, leading to bacterial growth inhibition and cell death [96]. Another proposed mechanism is that the NiSe NPs can penetrate bacterial cells and interact with intracellular components such as DNA and proteins, causing damage and impairing bacterial function. Additionally, some studies have suggested that the antibacterial activity of the NiSe NPs is related to factors such as their size, shape, and surface charge, as well as the bacterial species and environmental conditions [97]. Further research is needed to fully understand the antibacterial mechanism of the NiSe NPs and to optimize their antibacterial properties for various applications. The zone of inhibition of the NiSe NPs is depicted in Figure 9. The mechanism of antimicrobial activities of the green synthesized NiSe NPs is illustrated in Figure 10.

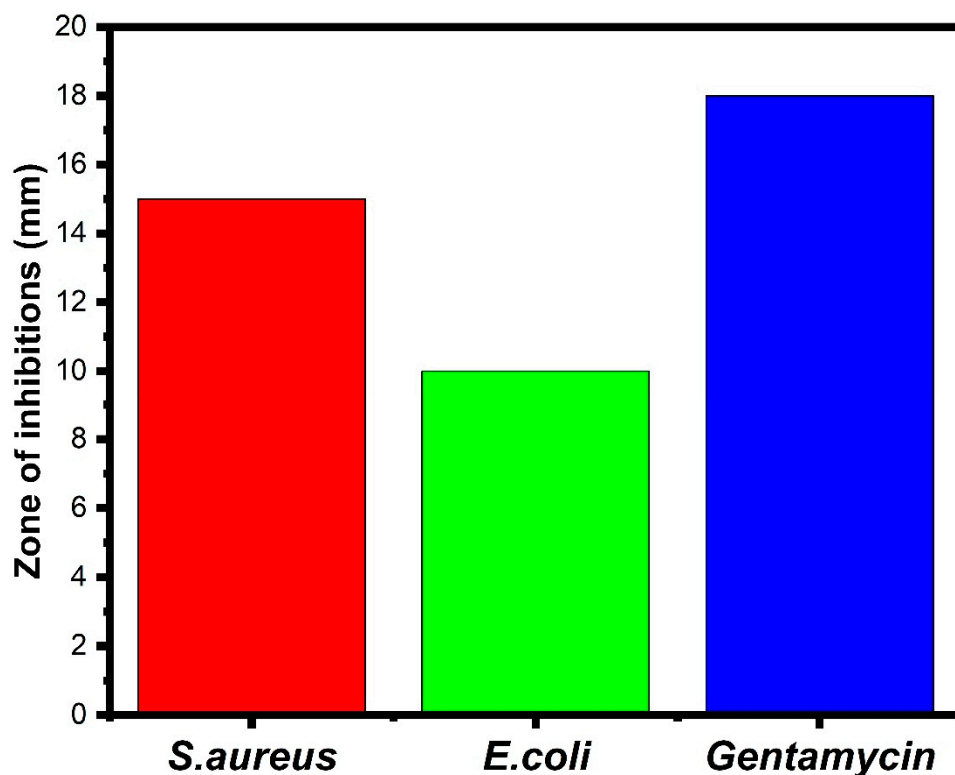


Figure 9. Antibacterial inhibitions plots of NiSe NPs.

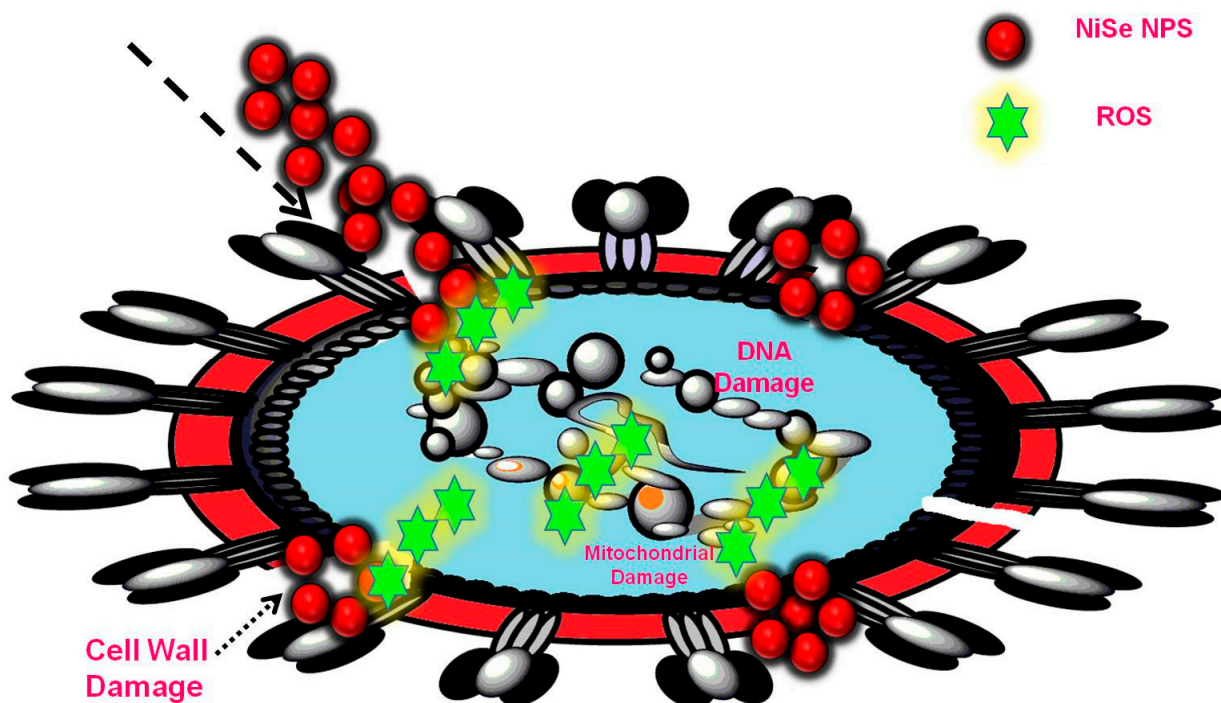


Figure 10. Antimicrobial activity mechanism of NiSe NPs.

4. Conclusions

We concluded that the structural, morphological, photocatalytic, and antimicrobial properties of NiSe NPs synthesized using the green method. The XRD, FTIR, EDAX, and FE-SEM clearly show the homogeneous formation of the NiSe NPs. The photocatalytic results show that the NiSe NPs degrade 92% of the MB dye in 120 min using simulated solar

radiation, indicating good degradation ability. A kinetic analysis reveals that the photo degradation of the NiSe NPs obtained the enhanced degradation under light irradiation. The investigation of antibacterial activity reveals that the NiSe NPs have higher resistivity toward *E. coli* and *S. aureus*, with the greatest inhibition of bacterial growth. The generated charge carriers, ROS, Ni²⁺ and Se²⁻ ions are deliberately attacking the bacterial toxins and the MB dye. In conclusion, the smaller crystallite size (24 nm), narrow bandgap (1.74 eV), valency of Ni-2p, Se-3d, and spherical morphology of the green synthesized NiSe NPs could be a better replacement for various microbial resistant activities, and it may be a viable approach for the complete removal of environmental pollutants.

5. Future Works

NiSe NPs have shown promising results in photocatalytic water treatment applications, but there is potential for their use in other areas such as air purification, solar energy conversion, and waste remediation. Further investigation is needed to determine the effectiveness of the NiSe NPs in these applications and optimize their performance. The NiSe NPs have demonstrated antimicrobial properties, making them a potential candidate for use in medical applications such as wound dressings or implant coatings. Further research is necessary to evaluate their effectiveness and safety for use in such applications. The NiSe NPs have unique electronic properties that make them a potential candidate for use in energy storage applications such as batteries and supercapacitors. Investigation into their performance in these applications and optimization of their properties is necessary to fully realize their potential. The NiSe NPs have shown promise as a catalyst in various chemical reactions, including hydrogen evolution, CO₂ reduction, and organic synthesis. Further investigation is necessary to optimize their performance and explore their potential in other catalytic reactions. As with any new material, it is important to study the potential toxicity of the NiSe NPs in vivo and in vitro to evaluate their safety for human and environmental exposure. The synthesis of the NiSe NPs at a large scale while maintaining their properties and reducing production costs is an important consideration for their potential commercialization. Research into scalable and cost-effective synthesis methods is necessary to enable their widespread use.

Author Contributions: Conceptualization, L.V. and M.J.; Data curation, L.V., C.P. and K.M.; Formal analysis, L.V.; Funding acquisition, J.K.G., S.M.W., S.A., M.R.S. and W.-C.L.; Investigation, L.V., J.K.G., S.M.W., S.A., M.R.S. and M.J.; Methodology, L.V.; Project administration, K.M. and M.J.; Resources, W.-C.L.; Software, D.C.A., K.M. and J.K.G., S.M.W., S.A., M.R.S.; Supervision, M.J.; Validation, M.J.; Visualization, M.J.; Writing—original draft, L.V. and C.P.; Writing—review & editing, L.V., C.P. and M.J. All authors have read and agreed to the published version of the manuscript.

Funding: The authors are grateful to the Researchers Supporting Project No. (RSP2023R326), King Saud University, Riyadh, Saudi Arabia.

Institutional Review Board Statement: Not applicable.

Informed Consent Statement: Not applicable.

Data Availability Statement: All research data are provided in the manuscript.

Acknowledgments: The authors are grateful to the Researchers Supporting Project No. (RSP2023R326), King Saud University, Riyadh, Saudi Arabia. Lakshmi Velayutham thanks the St. Xavier's College (Autonomous), Palayamkottai, Tirunelveli-627002 and Manonmaniam Sundaranar University, Tirunelveli-627012, Tamilnadu, India.

Conflicts of Interest: The authors declare no conflict of interest.

References

1. Clark, M. (Ed.) *Handbook of Textile and Industrial Dyeing: Principles, Processes and Types of Dyes*; Elsevier: Amsterdam, The Netherlands, 2011.
2. Salleh, M.A.M.; Mahmoud, D.K.; Karim, W.A.W.A.; Idris, A. Cationic and anionic dye adsorption by agricultural solid wastes: A comprehensive review. *Desalination* **2011**, *280*, 1–13. [[CrossRef](#)]

3. Khan, I.; Saeed, K.; Zekker, I.; Zhang, B.; Hendi, A.H.; Ahmad, A.; Ahmad, S.; Zada, N.; Ahmad, H.; Shah, L.A.; et al. Review on Methylene Blue: Its Properties, Uses, Toxicity and Photodegradation. *Water* **2022**, *14*, 242. [[CrossRef](#)]
4. Mansour, A.T.; Alprol, A.E.; Abualnaja, K.M.; El-Beltagi, H.S.; Ramadan, K.M.A.; Ashour, M. Dried Brown Seaweed's Phytoremediation Potential for Methylene Blue Dye Removal from Aquatic Environments. *Polymers* **2022**, *14*, 1375. [[CrossRef](#)] [[PubMed](#)]
5. Curteanu, S.; Piuleac, C.G.; Godini, K.; Azaryan, G. Modeling of electrolysis process in wastewater treatment using different types of neural networks. *Chem. Eng. J.* **2011**, *172*, 267–276. [[CrossRef](#)]
6. Henze, M.; van Loosdrecht, M.C.; Ekama, G.A.; Brdjanovic, D. (Eds.) *Biological Wastewater Treatment*; IWA Publishing: London, UK, 2008.
7. Zhao, C.; Zhou, J.; Yan, Y.; Yang, L.; Xing, G.; Li, H.; Wu, P.; Wang, M.; Zheng, H. Application of coagulation/flocculation in oily wastewater treatment: A review. *Sci. Total. Environ.* **2020**, *765*, 142795. [[CrossRef](#)]
8. Wang, J.; Chen, H. Catalytic ozonation for water and wastewater treatment: Recent advances and perspective. *Sci. Total. Environ.* **2019**, *704*, 135249. [[CrossRef](#)]
9. Abdel-Fatah, M.A. Nanofiltration systems and applications in wastewater treatment: Review article. *Ain Shams Eng. J.* **2018**, *9*, 3077–3092. [[CrossRef](#)]
10. Deng, Y.; Zhao, R. Advanced Oxidation Processes (AOPs) in Wastewater Treatment. *Curr. Pollut. Rep.* **2015**, *1*, 167–176. [[CrossRef](#)]
11. Russo, V.; Hmoudah, M.; Broccoli, F.; Iesce, M.R.; Jung, O.-S.; Di Serio, M. Applications of Metal Organic Frameworks in Wastewater Treatment: A Review on Adsorption and Photodegradation. *Front. Chem. Eng.* **2020**, *2*, 581487. [[CrossRef](#)]
12. Tyagi, V.K.; Lo, S.-L. Application of physico-chemical pretreatment methods to enhance the sludge disintegration and subsequent anaerobic digestion: An up to date review. *Rev. Environ. Sci. Bio. Technol.* **2011**, *10*, 215–242. [[CrossRef](#)]
13. Xiao, M.; Wang, Z.; Lyu, M.; Luo, B.; Wang, S.; Liu, G.; Cheng, H.-M.; Wang, L. Hollow nanostructures for photocatalysis: Advantages and challenges. *Adv. Mater.* **2019**, *31*, 1801369. [[CrossRef](#)] [[PubMed](#)]
14. Akpan, U.G.; Hameed, B.H. Parameters affecting the photocatalytic degradation of dyes using TiO₂-based photocatalysts: A review. *J. Hazard. Mater.* **2009**, *170*, 520–529. [[CrossRef](#)] [[PubMed](#)]
15. Mahato, N.; Sharma, K.; Sinha, M.; Baral, E.R.; Koteswararao, R.; Dhyani, A.; Cho, M.H.; Cho, S. Bio-sorbents, industrially important chemicals and novel materials from citrus processing waste as a sustainable and renewable bioresource: A review. *J. Adv. Res.* **2020**, *23*, 61–82. [[CrossRef](#)] [[PubMed](#)]
16. Yang, J.; Liu, D.; Song, X.; Zhao, Y.; Wang, Y.; Rao, L.; Fu, L.; Wang, Z.; Yang, X.; Li, Y.; et al. Recent Progress of Cellulose-Based Hydrogel Photocatalysts and Their Applications. *Gels* **2022**, *8*, 270. [[CrossRef](#)] [[PubMed](#)]
17. Batistela, V.R.; Fogaça, L.Z.; Fávoro, S.L.; Caetano, W.; Fernandes-Machado NR, C.; Hioka, N. ZnO supported on zeolites: Photocatalyst design, microporosity and properties. *Colloids Surf. A Physicochem. Eng. Asp.* **2017**, *513*, 20–27. [[CrossRef](#)]
18. Tian, C.; Zhang, Q.; Wu, A.; Jiang, M.; Liang, Z.; Jiang, B.; Fu, H. Cost-effective large-scale synthesis of ZnO photocatalyst with excellent performance for dye photodegradation. *Chem. Commun.* **2012**, *48*, 2858–2860. [[CrossRef](#)]
19. Sun, C.; Yang, J.; Xu, M.; Cui, Y.; Ren, W.; Zhang, J.; Zhao, H.; Liang, B. Recent intensification strategies of SnO₂-based photocatalysts: A review. *Chem. Eng. J.* **2021**, *427*, 131564. [[CrossRef](#)]
20. Cheng, L.; Xiang, Q.; Liao, Y.; Zhang, H. CdS-based photocatalysts. *Energy Environ. Sci.* **2018**, *11*, 1362–1391. [[CrossRef](#)]
21. Lee, G.-J.; Wu, J.J. Recent developments in ZnS photocatalysts from synthesis to photocatalytic applications—A review. *Powder Technol.* **2017**, *318*, 8–22. [[CrossRef](#)]
22. Sobhani, A.; Salavati-Niasari, M. Transition metal selenides and diselenides: Hydrothermal fabrication, investigation of morphology, particle size and their applications in photocatalyst. *Adv. Colloid Interface Sci.* **2021**, *287*, 102321. [[CrossRef](#)]
23. Frame, F.A.; Carroll, E.C.; Larsen, D.S.; Sarahan, M.; Browning, N.D.; Osterloh, F.E. First demonstration of CdSe as a photocatalyst for hydrogen evolution from water under UV and visible light. *Chem. Commun.* **2008**, *19*, 2206–2208. [[CrossRef](#)]
24. Zhang, L.; Yang, H.; Xie, X.; Zhang, F.; Li, L. Preparation and photocatalytic activity of hollow ZnSe microspheres via Ostwald ripening. *J. Alloys Compd.* **2009**, *473*, 65–70. [[CrossRef](#)]
25. Győri, Z.; Kónya, Z.; Kukovecz, Á. Visible light activation photocatalytic performance of PbSe quantum dot sensitized TiO₂ Nanowires. *Appl. Catal. B Environ.* **2015**, *179*, 583–588. [[CrossRef](#)]
26. Li, J.; Yang, M.; Feng, Z.; Lan, F.; Teng, C.; Li, D.; Tang, J. A new HgSe photocatalyst for degradation of organic dyes under visible light irradiation. *Mater. Lett.* **2015**, *161*, 591–594. [[CrossRef](#)]
27. Khan, M.; Khan, A.; Khan, H.; Ali, N.; Sartaj, S.; Malik, S.; Ali, N.; Khan, H.; Shah, S.; Bilal, M. Development and characterization of regenerable chitosan-coated nickel selenide nano-photocatalytic system for decontamination of toxic azo dyes. *Int. J. Biol. Macromol.* **2021**, *182*, 866–878. [[CrossRef](#)] [[PubMed](#)]
28. Hopkins, M.A.; Kuperman, N.; Barnes, J.; Solanki, R. Magnetic Characterization of Cobalt Selenide and Nickel Selenide Thin Films. In Proceedings of the 2018 IEEE 13th Nanotechnology Materials and Devices Conference (NMDC), Portland, OR, USA, 14–17 October 2018; pp. 1–4.
29. Hankare, P.; Jadhav, B.; Garadkar, K.; Chate, P.; Mulla, I.; Delekar, S. Synthesis and characterization of nickel selenide thin films deposited by chemical method. *J. Alloys Compd.* **2010**, *490*, 228–231. [[CrossRef](#)]
30. Tito, G.S.; Abolanle, A.S.; Kuvarega, A.T.; Idris, A.O.; Mamba, B.B.; Feloni, U. Nickel selenide quantum dot applications in electrocatalysis and sensors. *Electroanalysis* **2020**, *32*, 2603–2614. [[CrossRef](#)]

31. Du, L.; Du, W.; Ren, H.; Wang, N.; Yao, Z.; Shi, X.; Zhang, B.; Zai, J.; Qian, X. Honeycomb-like metallic nickel selenide nanosheet arrays as binder-free electrodes for high-performance hybrid asymmetric supercapacitors. *J. Mater. Chem. A* **2017**, *5*, 22527–22535. [[CrossRef](#)]
32. Rahman, M.A.; Radhakrishnan, R. Microstructural properties and antibacterial activity of Ce doped NiO through chemical method. *SN Appl. Sci.* **2019**, *1*, 221. [[CrossRef](#)]
33. Ramakrishnan, P.; Jo, S.; Pitipuech, N.; Sohn, J.I. Bifunctionality behavior of phase controlled nickel selenides in alkaline water electrolysis application. *Electrochim. Acta* **2020**, *354*, 136742. [[CrossRef](#)]
34. Divya, R.; Manikandan, N.; Vinitha, G. Synthesis and characterization of nickel doped zinc selenide nanospheres for nonlinear optical applications. *J. Alloys Compd.* **2019**, *791*, 601–612. [[CrossRef](#)]
35. Wei, P.; Li, J.; Kang, H.; Yang, Y.; Hao, Z.; Chen, X.; Guo, D.; Liu, L. Facile synthesis and promising application of iron-doped nickel selenide nanoparticles as high-efficiency counter electrodes of dye-sensitized solar cells. *Int. J. Energy Res.* **2019**, *44*, 845–854. [[CrossRef](#)]
36. Philip, D. Green synthesis of gold and silver nanoparticles using *Hibiscus rosa sinensis*. *Physica E Low Dimens. Syst. Nanostruct.* **2010**, *42*, 1417. [[CrossRef](#)]
37. Nayak, D.; Ashe, S.; Rauta, P.R.; Nayak, B. Biosynthesis, characterisation and antimicrobial activity of silver nanoparticles using *Hibiscus rosa-sinensis* petals extracts. *IET Nanobiotechnology* **2015**, *9*, 288–293. [[CrossRef](#)] [[PubMed](#)]
38. Chai, H.-Y.; Lam, S.-M.; Sin, J.-C. Green synthesis of magnetic Fe-doped ZnO nanoparticles via *Hibiscus rosa-sinensis* leaf extracts for boosted photocatalytic, antibacterial and antifungal activities. *Mater. Lett.* **2019**, *242*, 103–106. [[CrossRef](#)]
39. Anuradha, C.T.; Raji, P. Effect of annealing temperature on antibacterial, antifungal and structural properties of bio-synthesized Co₃O₄ nanoparticles using *Hibiscus Rosa-sinensis*. *Mater. Res. Express* **2019**, *6*, 095063. [[CrossRef](#)]
40. Lu, L.; Zhuang, Z.; Fan, M.; Liu, B.; Yang, Y.; Huang, J.; Da, X.; Mo, J.; Li, Q.; Lu, H. Green formulation of Ag nanoparticles by *Hibiscus rosa-sinensis*: Introducing a navel chemotherapeutic drug for the treatment of liver cancer. *Arab. J. Chem.* **2021**, *15*, 103602. [[CrossRef](#)]
41. Buarki, F.; AbuHassan, H.; Al Hannan, F.; Henari, F.Z. Green Synthesis of Iron Oxide Nanoparticles Using *Hibiscus rosa sinensis* Flowers and Their Antibacterial Activity. *J. Nanotechnol.* **2022**, *2022*, 5474645. [[CrossRef](#)]
42. Kumar, B.; Smita, K.; Angulo, Y.; Debut, A.; Cumbal, L. China Rose/*Hibiscus rosa-sinensis* Pollen-Mediated Phytosynthesis of Silver Nanoparticles and Their Catalytic Activity. *J. Compos. Sci.* **2022**, *6*, 322. [[CrossRef](#)]
43. Mughilmathi; Sonali, J.M.I.; Kumar, P.S.; Archana, K.M.; Rajagopal, R.; Gayathri, K.V. Application of copper iodide (CuI) and natural dye extracted from *Hibiscus rosa-sinensis* onto cotton fabric: An integrated approach. *Appl. Nanosci.* **2022**, 1–10. [[CrossRef](#)]
44. Sampath, S.; Bhushan, M.; Saxena, V.; Pandey, L.M.; Singh, L.R. Green synthesis of Ag doped ZnO nanoparticles: Study of their structural, optical, thermal and antibacterial properties. *Mater. Technol.* **2022**, *37*, 2785–2794. [[CrossRef](#)]
45. Nachimuthu, S.; Thangavel, S.; Kannan, K.; Selvakumar, V.; Muthusamy, K.; Siddiqui, M.R.; Wabaidur, S.M.; Parvathiraja, C. Lawsonia inermis mediated synthesis of ZnO/Fe₂O₃ nanorods for photocatalysis–Biological treatment for the enhanced effluent treatment, antibacterial and antioxidant activities. *Chem. Phys. Lett.* **2022**, *804*, 139907. [[CrossRef](#)]
46. Mansour, A.T.; Alprol, A.E.; Khedawy, M.; Abualnaja, K.M.; Shalaby, T.A.; Rayan, G.; Ramadan, K.M.A.; Ashour, M. Green Synthesis of Zinc Oxide Nanoparticles Using Red Seaweed for the Elimination of Organic Toxic Dye from an Aqueous Solution. *Materials* **2022**, *15*, 5169. [[CrossRef](#)] [[PubMed](#)]
47. Tito, G.S.; Kuvarega, A.T.; Mamba, B.B.; Feloni, U. Electrochemical Detection of Nevirapine Using Banana Peel Extract Functionalised Nickel Selenide Quantum Dots. *Electrocatalysis* **2022**, *14*, 393–405. [[CrossRef](#)]
48. Parvathiraja, C.; Katheria, S.; Siddiqui, M.R.; Wabaidur, S.M.; Islam, A.; Lai, W.-C. Activated Carbon-Loaded Titanium Dioxide Nanoparticles and Their Photocatalytic and Antibacterial Investigations. *Catalysts* **2022**, *12*, 834. [[CrossRef](#)]
49. Al-Hada, N.M.; Kasmani, R.M.; Kasim, H.; Al-Ghaili, A.M.; Saleh, M.A.; Baqiah, H.; Al-Asbahi, B.A.; Yang, J.; Noorazlan, A.M.; Li, Q.; et al. Up-scalable synthesis of size-controlled NiSe nanoparticles using single step technique. *J. Mater. Res. Technol.* **2022**, *18*, 4918–4929. [[CrossRef](#)]
50. Tian, Y.; Wu, Y.; Liang, H.; Zhao, B.; Jin, Y.; Liu, J.; Li, Z. Bimetal selenide NiSe/ZnSe heterostructured nanoparticles decorated porous g-C₃N₄ nanosheets to boost H₂ evolution and urea synthesis. *Appl. Surf. Sci.* **2022**, *602*, 154329. [[CrossRef](#)]
51. Zeng, R.; Cheng, C.; Xing, F.; Zou, Y.; Ding, K.; Huang, C. Dual vacancies induced local polarization electric field for high-performance photocatalytic H₂ production. *Appl. Catal. B Environ.* **2022**, *316*, 121680. [[CrossRef](#)]
52. Jia, J.; Zheng, L.; Li, K.; Zhang, Y.; Xie, H. Two-electron transfer mechanism from 3D/3D nickel selenide/MoS₂ heterostructure accelerates photocatalytic hydrogen evolution and tetracycline hydrochloride removal. *Chem. Eng. J.* **2022**, *429*, 132432. [[CrossRef](#)]
53. Li, M.; Wang, J.; Liao, J.; Wang, L.; Ju, Y.; Wang, X.; Wei, J.; Hu, N.; Xu, R.; Yang, L. NiSe@Ni₁₂P₅ hierarchical nanorod arrays coupled on nickel-copper foam for highly efficient urea oxidation. *Appl. Surf. Sci.* **2023**, *607*, 155041. [[CrossRef](#)]
54. Xu, X.; Wang, R.; Chen, S.; Trukhanov, A.; Wu, Y.; Shao, L.; Heng, L.; Sun, Z. Interface engineering of hierarchical P-doped NiSe/2H-MoS₂ nanorod arrays for efficient hydrogen evolution. *Inorg. Chem. Front.* **2022**, *9*, 5507–5516. [[CrossRef](#)]
55. Wang, L.; Lu, Y.; Xie, M.; Zhao, S.; Li, Z.; Liu, Q. Interfacially engineered induced nickel-based heterostructures as efficient catalysts for Li-O₂ batteries. *Electrochim. Acta* **2023**, *437*, 141476. [[CrossRef](#)]
56. Manickam, S.; Kuzhandaivel, H.; Selvaraj, Y.; Franklin, M.C.; Nallathambi, K.S. One-pot synthesis of TEA functionalized and NiSe embedded rGO nanocomposites for supercapacitor application. *Dalton Trans.* **2022**, *51*, 1542–1552. [[CrossRef](#)] [[PubMed](#)]

57. Mohammadi, M.A.; Yazdi, M.S.; Noghani, M.T.; Moghanian, A.; Hosseini, S.A. Synthesis and optimization of Mo–Ni–Se@NiSe core-shell nanostructures as efficient and durable electrocatalyst for hydrogen evolution reaction in alkaline media. *Int. J. Hydrogen Energy* **2022**, *47*, 34455–34470. [[CrossRef](#)]
58. Cao, Y.; Lei, F.; Li, Y.; Fu, Y.; Zhao, J.; Qiu, S.; Zhang, Z. Interface engineering in NiSe₂/Ni₂Co/CoSe₂ heterostructures encapsulated in hollow carbon shells for high-rate Li–Se batteries. *Nanoscale* **2022**, *14*, 13227–13235. [[CrossRef](#)] [[PubMed](#)]
59. Balaji, D.; Arunachalam, P.; Duraimurugan, K.; Madhavan, J.; Theerthagiri, J.; Al-Mayouf, A.M.; Choi, M.Y. Highly efficient Ni_{0.5}Fe_{0.5}Se₂/MWCNT electrocatalyst for hydrogen evolution reaction in acid media. *Int. J. Hydrogen Energy* **2020**, *45*, 7838–7847. [[CrossRef](#)]
60. Hussain, R.A.; Hussain, I. Fabrication and applications of nickel selenide. *J. Solid State Chem.* **2019**, *277*, 316–328. [[CrossRef](#)]
61. Khan, B.A.; Hussain, R.; Shah, A.; Mahmood, A.; Shah, M.Z.U.; Ismail, J.; Rahman, S.U.; Sajjad, M.; Assiri, M.A.; Imran, M.; et al. NiSe₂ nanocrystals intercalated rGO sheets as a high-performance asymmetric supercapacitor electrode. *Ceram. Int.* **2022**, *48*, 5509–5517. [[CrossRef](#)]
62. Wang, Y.; Torres, J.A.; Shviro, M.; Carmo, M.; He, T.; Ribeiro, C. Photocatalytic materials applications for sustainable agriculture. *Prog. Mater. Sci.* **2022**, *130*, 100965. [[CrossRef](#)]
63. Nabi, G.; Ain, Q.-U.; Tahir, M.B.; Riaz, K.N.; Iqbal, T.; Rafique, M.; Hussain, S.; Raza, W.; Aslam, I.; Rizwan, M. Green synthesis of TiO₂ nanoparticles using lemon peel extract: Their optical and photocatalytic properties. *Int. J. Environ. Anal. Chem.* **2020**, *102*, 434–442. [[CrossRef](#)]
64. Mahdavi, K.; Zinatloo-Ajabshir, S.; Yousif, Q.A.; Salavati-Niasari, M. Enhanced photocatalytic degradation of toxic contaminants using Dy₂O₃-SiO₂ ceramic nanostructured materials fabricated by a new, simple and rapid sonochemical approach. *Ultrason. Sonochem.* **2021**, *82*, 105892. [[CrossRef](#)] [[PubMed](#)]
65. Ravele, M.P.; Oyewo, O.A.; Ramaila, S.; Mavuru, L.; Onwudiwe, D.C. Facile synthesis of copper oxide nanoparticles and their applications in the photocatalytic degradation of acyclovir. *Results Eng.* **2022**, *14*, 100479. [[CrossRef](#)]
66. Lv, C.; Zhang, T.; Wang, X.; Pan, H.; Xie, Z.; Lu, H.; Pan, K.; Xie, Y. Enhancement of the triiodide reduction reaction by doping molybdenum in NiSe hierarchical microspheres: A theoretical and experimental study. *Inorg. Chem. Front.* **2022**, *10*, 460–467. [[CrossRef](#)]
67. Gan, Y.; Li, Z.; Ye, Y.; Dai, X.; Nie, F.; Yin, X.; Ren, Z.; Wu, B.; Cao, Y.; Cai, R.; et al. Doping Mo into NiFe LDH/NiSe Heterostructure to Enhance Oxygen Evolution Activity by Synergistically Facilitating Electronic Modulation and Surface Reconstruction. *ChemSusChem* **2022**, *15*, e202201205. [[CrossRef](#)] [[PubMed](#)]
68. Zhu, F.-Y.; Zhang, X.; Han, X.; Zhou, C.; Lu, S.; Lang, J.-P.; Gu, H. Nanostructured catalyst assembled from CNTs, NiSe₂ nanoparticles, and 2D Ni-MOF nanosheets for electrocatalytic hydrogen evolution reaction. *CrystEngComm* **2022**, *24*, 8503–8508. [[CrossRef](#)]
69. Xin, Y.; Nie, S.; Pan, S.; Miao, C.; Mou, H.; Wen, M.; Xiao, W. Electrospinning fabrication of Sb-SnSb/TiO₂@CNFs composite nanofibers as high-performance anodes for lithium-ion batteries. *J. Colloid Interface Sci.* **2022**, *630*, 403–414. [[CrossRef](#)]
70. Bao, W.; Yang, C.; Ai, T.; Zhang, J.; Zhou, L.; Yan, L.; Wei, X.; Zou, X.; Wang, Y. Modulating interfacial charge distribution of NiSe nanoarrays with NiFe-LDH nanosheets for boosting oxygen evolution reaction. *Fuel* **2023**, *332*, 126227. [[CrossRef](#)]
71. Chang, K.; Tran, D.T.; Wang, J.; Kim, N.H.; Lee, J.H. A 3D hierarchical network derived from 2D Fe-doped NiSe nanosheets/carbon nanotubes with enhanced OER performance for overall water splitting. *J. Mater. Chem. A* **2021**, *10*, 3102–3111. [[CrossRef](#)]
72. Wang, D.; Li, L.; Liu, Z.; Gao, S.; Zhang, G.; Hou, Y.; Wen, G.; Zhang, L.; Gu, H.; Zhang, R. A unique two-phase heterostructure with cubic NiSe₂ and orthorhombic NiSe₂ for enhanced lithium ion storage and electrocatalysis. *Dalton Trans.* **2022**, *51*, 12829–12838. [[CrossRef](#)] [[PubMed](#)]
73. Zhai, X.; Pang, X.; Wang, X.; Xu, H.; Zhang, C.; Zhang, Q.; Zhou, Y.; Tian, L. Facile fabrication of hydrangea-like NiSe/FeSe₂ nanostructures towards efficient water oxidation. *J. Saudi Chem. Soc.* **2022**, *26*, 101469. [[CrossRef](#)]
74. Yuan, Y.; Wu, Y.; Suganthy, N.; Shanmugam, S.; Brindhadevi, K.; Sabour, A.; Alshiekheid, M.; Chi, N.T.L.; Pugazhendhi, A.; Shanmuganathan, R. Biosynthesis of zirconium nanoparticles (ZrO₂ NPs) by Phyllanthus niruri extract: Characterization and its photocatalytic dye degradation activity. *Food Chem. Toxicol.* **2022**, *168*, 113340. [[CrossRef](#)] [[PubMed](#)]
75. Shelke, H.D.; Machale, A.R.; Survase, A.A.; Pathan, H.M.; Lokhande, C.D.; Lokhande, A.C.; Shaikh, S.F.; Rana, A.U.H.S.; Palaniswami, M. Multifunctional Cu₂SnS₃ Nanoparticles with Enhanced Photocatalytic Dye Degradation and Antibacterial Activity. *Materials* **2022**, *15*, 3126. [[CrossRef](#)]
76. Tantubay, K.; Das, P.; Baskey, M. Hydrogen peroxide-assisted photocatalytic dye degradation over reduced graphene oxide integrated ZnCr₂O₄ nanoparticles. *Environ. Sci. Pollut. Res.* **2021**, *29*, 17309–17318. [[CrossRef](#)] [[PubMed](#)]
77. Jasrotia, R.; Kumari, N.; Kumar, R.; Naushad, M.; Dhiman, P.; Sharma, G. Photocatalytic degradation of environmental pollutant using nickel and cerium ions substituted Co_{0.6}Zn_{0.4}Fe₂O₄ nanoferrites. *Earth Syst. Environ.* **2021**, *5*, 399–417. [[CrossRef](#)]
78. Qin, L.; Li, Y.; Liang, F.; Li, L.; Lan, Y.; Li, Z.; Lu, X.; Yang, M.; Ma, D. A microporous 2D cobalt-based MOF with pyridyl sites and open metal sites for selective adsorption of CO₂. *Microporous Mesoporous Mater.* **2022**, *341*, 112098. [[CrossRef](#)]
79. Qin, L.; Liang, F.; Li, Y.; Wu, J.; Guan, S.; Wu, M.; Xie, S.; Luo, M.; Ma, D. A 2D Porous Zinc-Organic Framework Platform for Loading of 5-Fluorouracil. *Inorganics* **2022**, *10*, 202. [[CrossRef](#)]
80. Dong, X.; Li, Y.; Li, D.; Liao, D.; Qin, T.; Prakash, O.; Kumar, A.; Liu, J.-Q. A new 3D 8-connected Cd(ii) MOF as a potent photocatalyst for oxytetracycline antibiotic degradation. *CrystEngComm* **2022**, *24*, 6933–6943. [[CrossRef](#)]

81. Zheng, M.; Chen, J.; Zhang, L.; Cheng, Y.; Lu, C.; Liu, Y.; Singh, A.; Trivedi, M.; Kumar, A.; Liu, J. Metal organic frameworks as efficient adsorbents for drugs from wastewater. *Mater. Today Commun.* **2022**, *31*, 103514. [[CrossRef](#)]
82. Rao, C.; Zhou, L.; Pan, Y.; Lu, C.; Qin, X.; Sakiyama, H.; Muddassir, M.; Liu, J. The extra-large calixarene-based MOFs-derived hierarchical composites for photocatalysis of dye: Facile syntheses and contribution of carbon species. *J. Alloys Compd.* **2021**, *897*, 163178. [[CrossRef](#)]
83. Zhong, Y.; Chen, C.; Liu, S.; Lu, C.; Liu, D.; Pan, Y.; Sakiyama, H.; Muddassir, M.; Liu, J. A new magnetic adsorbent of eggshell-zeolitic imidazolate framework for highly efficient removal of norfloxacin. *Dalton Trans.* **2021**, *50*, 18016–18026. [[CrossRef](#)]
84. Oh, W.-C.; Ullah, K.; Zhu, L.; Meng, Z.-D.; Ye, S.; Sarkar, S. Photocatalytic properties under visible light with graphene based platinum selenide nanocomposites synthesized by microwave assisted method. *Mater. Sci. Semicond. Process.* **2014**, *25*, 34–42. [[CrossRef](#)]
85. Beena, V.; Ajitha, S.; Rayar, S.L.; Parvathiraja, C.; Kannan, K.; Palani, G. Enhanced Photocatalytic and Antibacterial Activities of ZnSe Nanoparticles. *J. Inorg. Organomet. Polym. Mater.* **2021**, *31*, 4390–4401. [[CrossRef](#)]
86. Ahmad, W.; Khan, A.; Ali, N.; Khan, S.; Uddin, S.; Malik, S.; Ali, N.; Khan, H.; Khan, H.; Bilal, M. Photocatalytic degradation of crystal violet dye under sunlight by chitosan-encapsulated ternary metal selenide microspheres. *Environ. Sci. Pollut. Res.* **2020**, *28*, 8074–8087. [[CrossRef](#)] [[PubMed](#)]
87. Firdaus, F.; E Iram, N.; Khan, M.S.; Baig, U. Facile Synthesis, Characterization and Photocatalytic Activity of Band Gap Engineered Cobalt Selenide Nanoparticles. *Arab. J. Sci. Eng.* **2016**, *41*, 2377–2384. [[CrossRef](#)]
88. Ahmed, M.K.; Shalan, A.E.; Afifi, M.; El-Desoky, M.M.; Lanceros-Méndez, S. Silver-doped cadmium selenide/graphene oxide-filled cellulose acetate nanocomposites for photocatalytic degradation of malachite green toward wastewater treatment. *ACS Omega* **2021**, *6*, 23129–23138. [[CrossRef](#)]
89. Ashiq, M.N.; Irshad, S.; Ehsan, M.F.; Rehman, S.; Farooq, S.; Najam-Ul-Haq, M.; Zia, A. Visible-light active tin selenide nanostructures: Synthesis, characterization and photocatalytic activity. *New J. Chem.* **2017**, *41*, 14689–14695. [[CrossRef](#)]
90. Cheng, Y.; Zhang, J.; Xiong, X.; Chen, C.; Zeng, J.; Kong, Z.; Wang, H.; Xi, J.; Yuan, Y.-J.; Ji, Z. High photocatalytic and photoelectrochemical performances of the CuSe/MoSe₂ 2D/2D face-to-face heterojunction photocatalyst. *J. Alloys Compd.* **2021**, *870*, 159540. [[CrossRef](#)]
91. Patidar, D.; Yadav, A.; Paul, D.R.; Sharma, A.; Nehra, S. Nanohybrids cadmium selenide-reduced graphene oxide for improving photo-degradation of methylene blue. *Phys. E Low-Dimens. Syst. Nanostructures* **2019**, *114*, 113560. [[CrossRef](#)]
92. Ullah, K.; Ye, S.; Jo, S.-B.; Zhu, L.; Cho, K.-Y.; Oh, W.-C. Optical and photocatalytic properties of novel heterogeneous PtSe₂-graphene/TiO₂ nanocomposites synthesized via ultrasonic assisted techniques. *Ultrason. Sonochem.* **2014**, *21*, 1849–1857. [[CrossRef](#)]
93. Nguyen, V.K.; Pham, D.K.; Tran, N.Q.; Dang, L.H.; Nguyen, N.H.; Nguyen, T.V.; Nguyen, T.H.; Luong, T.B. Comparative Studies of Blue-Emitting Zinc Selenide Nanocrystals Doped with Ag, Cu, and Mg towards Medical Applications. *Crystals* **2022**, *12*, 625. [[CrossRef](#)]
94. Bootchanont, A.; Wechprasit, T.; Isran, N.; Theangsunthorn, J.; Chaosuan, N.; Chanlek, N.; Kidkhunthod, P.; Yimnirun, R.; Jiamprasertboon, A.; Eknapakul, T.; et al. Correlation of the antibacterial activity and local structure in Zn- and Mn-doped hydroxyapatites by Rietveld refinement and the first-principles method. *Materialia* **2022**, *26*, 101586. [[CrossRef](#)]
95. Roy, S.; Ezati, P.; Priyadarshi, R.; Biswas, D.; Rhim, J.W. Recent advances in metal sulfide nanoparticle-added bionanocomposite films for food packaging applications. *Crit. Rev. Food Sci. Nutr.* **2022**, *1–14*. [[CrossRef](#)] [[PubMed](#)]
96. Wang, C.; Xia, Y.; Wu, G.; Zhou, L.; Wei, S. Synthesis of sub-1 nm 2D transitional metal oxides via anion exchange-bonds cleavage cascade reactions. *Chem. Eng. J.* **2022**, *437*, 135230. [[CrossRef](#)]
97. Nieto-Maldonado, A.; Bustos-Guadarrama, S.; Espinoza-Gomez, H.; Flores-López, L.Z.; Ramirez-Acosta, K.; Alonso-Nuñez, G.; Cadena-Nava, R.D. Green synthesis of copper nanoparticles using different plant extracts and their antibacterial activity. *J. Environ. Chem. Eng.* **2022**, *10*, 107130. [[CrossRef](#)]

Disclaimer/Publisher’s Note: The statements, opinions and data contained in all publications are solely those of the individual author(s) and contributor(s) and not of MDPI and/or the editor(s). MDPI and/or the editor(s) disclaim responsibility for any injury to people or property resulting from any ideas, methods, instructions or products referred to in the content.